

# INSID3: Training-Free In-Context Segmentation with DINOv3

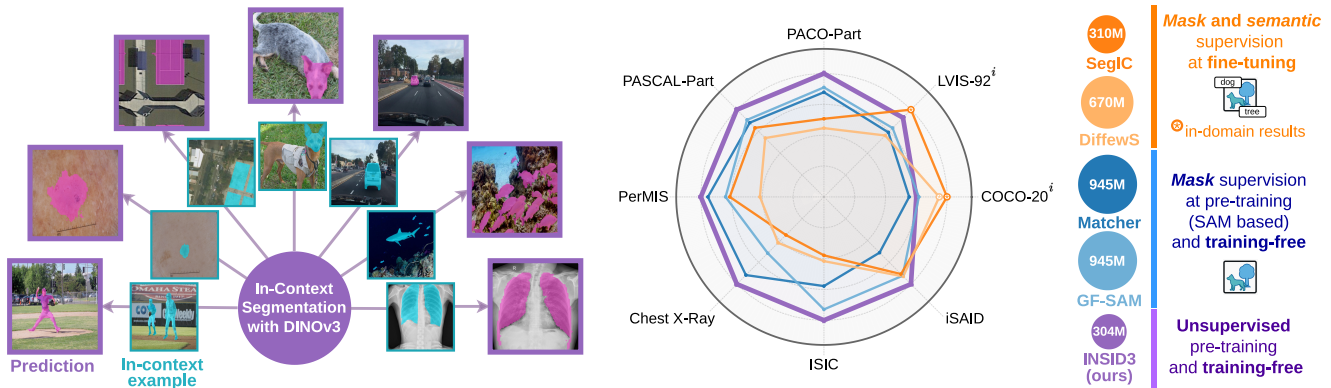
Claudia Cattano<sup>\*1,2</sup>Gabriele Trivigno<sup>\*1</sup>Christoph Reich<sup>2,3,5,6</sup>Daniel Cremers<sup>3,5,6</sup>Carlo Masone<sup>1</sup>Stefan Roth<sup>2,4,5</sup><sup>1</sup>Politecnico di Torino<sup>2</sup>TU Darmstadt<sup>3</sup>TU Munich<sup>4</sup>hessian.AI<sup>5</sup>ELIZA<sup>6</sup>MCML<sup>\*</sup>equal contribution
<https://visinf.github.io/INSID3>


Figure 1. **Results and overview of INSID3, our training-free in-context segmentation approach.** INSID3 performs in-context segmentation directly from DINOv3 [56] features, without any decoder, fine-tuning, or model composition. (left) A single annotated example guides the model to segment any concept, from object parts to medical images and aerial views. (right) Comparing generalization across datasets and segmentation granularities: fine-tuned methods (orange) excel in-domain (⊗) but degrade out of distribution, while SAM-based pipelines (blue) generalize better but rely on large, multi-stage architectures. INSID3 (purple) achieves the strongest generalization with a single backbone, revealing that robust segmentation can emerge directly from the dense self-supervised representations of DINOv3.

## Abstract

*In-context segmentation (ICS) aims to segment arbitrary concepts, e.g., objects, parts, or personalized instances, given one annotated visual examples. Existing work relies on (i) fine-tuning vision foundation models (VFMs), which improves in-domain results but harms generalization, or (ii) combines multiple frozen VFMs, which preserves generalization but yields architectural complexity and fixed segmentation granularities. We revisit ICS from a minimalist perspective and ask: Can a single self-supervised backbone support both semantic matching and segmentation, without any supervision or auxiliary models? We show that scaled-up dense self-supervised features from DINOv3 exhibit strong spatial structure and semantic correspondence. We introduce INSID3, a training-free approach that segments concepts at varying granularities only from frozen DINOv3 features, given an in-context example. INSID3 achieves state-of-the-art results across one-shot semantic, part, and personalized segmentation, outperforming previous work by +7.5% mIoU, while using 3× fewer parameters and without any mask or category-level supervision.*

## 1. Introduction

Understanding visual scenes is a fundamental task with applications in autonomous driving [11, 31], robotics [18], augmented reality [34], or medical image analysis [62]. In-context segmentation (ICS) [39, 41, 72] approaches the task of segmenting arbitrary concepts, such as *objects, parts, or personalized instances* in images, given one or more annotated examples at inference time, cf. Fig. 1 (left). This holistic and open-world scene understanding task requires adaptability to different reference annotations and domains, sharing the spirit of adapting large language models (LLMs) through contextual instructions to novel tasks [3, 9, 48, 58].

ICS requires reliable visual correspondences between annotated reference examples and target images. Previous work showed that such visual correspondences emerge in features of vision foundation models (VFMs) [57, 70]. Based on this, recent work has explored how to endow VFMs with explicit segmentation capabilities. For instance, [38, 41, 74] augment a frozen DINOv2 [47] by training a segmentation decoder on top or fine-tune a diffusion model [52] through episodic training. These approaches aim to

translate implicit visual understanding of VFMs into dense, pixel-level predictions. Although this boosts in-domain results, it requires additional supervision and narrows the model scope to the training distribution (*cf.* Fig. 1, *orange*).

In contrast, recent training-free approaches [39, 69] forego task-specific training, exploiting the complementary strengths of multiple pre-trained components: DINOv2 [47] for robust visual correspondence and SAM [33] for producing accurate masks. By relying purely on pre-trained models, these methods avoid the pitfalls of fine-tuning, achieving stronger generalization (Fig. 1, *blue*). Nevertheless, they need to coordinate multiple VFMs, add significant computational overhead, and cannot fully exploit the intrinsic synergy between correspondence and segmentation.

Overall, existing ICS methods rely explicitly or implicitly on segmentation priors learned through supervision, whether from SAM pre-training or downstream fine-tuning. The recent DINOv3 model [56] may hold the key to changing this. This purely self-supervised VFM, trained on massive-scale image corpora, is explicitly designed to produce dense localized features, unlike its predecessors [7, 47]. Its objective preserves spatial structure, enabling robust region-level grouping (Fig. 2). This urges us to ask if ICS can emerge directly from the DINOv3 representation, without any decoder, fine-tuning, or model composition.

To this end, we propose INSID3 (**In**-context **S**egmentation **w**ith **D**INOv**3**), a minimalist and training-free approach, relying solely on DINOv3 features. INSID3 operates in three conceptual stages: (i) *Fine-grained clustering* of target image features allows to obtain part-level region candidates (Fig. 2). (ii) *Seed-cluster selection* identifies the most discriminative cluster through cross-image similarity between a prototype of the annotated example(s) and each cluster in the target. Relying on region-level similarity suppresses spurious pixel matches and resolves competition among many candidates. (iii) *Aggregation guided by self-similarity* of DINOv3 features within the target image then merges the seed cluster with other highly affine clusters, producing a spatially coherent mask that recovers the full extent of the prompted concept.

Finally, we uncover a subtle, yet significant limitation of correspondences from DINOv3: feature similarities across unrelated images exhibit systematic activations aligned with absolute spatial coordinates (*e.g.*, features from the left side of two images tend to spuriously match regardless of semantics, as shown in Fig. 4). This *positional bias*, likely an effect of the superposition of positional encodings and semantic signals, hinders reliable correspondence reasoning in matching tasks. We propose a simple correction: we estimate the subspace affected by positional bias from a noise image and perform matching only in its orthogonal complement. This lightweight operation improves cross-image matching and, as we show, even generalizes beyond ICS.



Figure 2. **Region-level grouping from DINOv3.** Each pair shows an input image (*left*) and the corresponding clustering map (*right*) obtained by applying agglomerative clustering to dense DINOv3 features. The resulting clusters delineate coherent object- and part-level regions, providing a structured decomposition of the scene.

In summary, we propose INSID3, a principled, minimalist, yet accurate method for in-context segmentation from DINOv3 alone. It is applicable across diverse semantic granularities, *e.g.*, from *objects* to *parts*, and demonstrates that emergent segmentation behavior can arise naturally from self-supervision without any training or fine-tuning.

Summarizing, we make the following contributions:

- We are the first to show that *a self-supervised VFM suffices for training-free in-context segmentation*, building on DINOv3’s core strengths of robust correspondence and its dense, localized feature structure.
- Despite its simplicity, INSID3 *generalizes better across the board*, from traditional, challenging benchmarks to out-of-domain datasets and part segmentation (Fig. 1, *purple*), outperforming fine-tuned *and* training-free approaches relying on SAM by an average of +7.5 % mIoU.
- We unveil a *positional bias in DINOv3*, which impairs its effectiveness in matching features across images, and present a simple training-free correction that generalizes beyond ICS, achieving gains of up to +6.6 % PCK on the related task of semantic correspondence.

## 2. Related Work

**In-context segmentation** (ICS) draws inspiration from LLMs [3, 9, 48, 58], which can be adapted to new tasks given contextual examples. SegGPT [64] and Painter [63] translate this idea to computer vision by training a generalist model to handle multiple segmentation scenarios. Recently, this idea has been revisited in light of the advent of large-scale pre-trained VFMs: Matcher [39] uses an annotated example to perform one-shot *semantic* and *part* segmentation, while PerSAM [72] focuses on one-shot *personalized* segmentation. Although related in spirit to few-shot segmentation [12, 27, 37, 61], which learns from base classes and evaluates on disjoint novel ones defined within each dataset, ICS differs in scope and evaluation. In particular, we refer

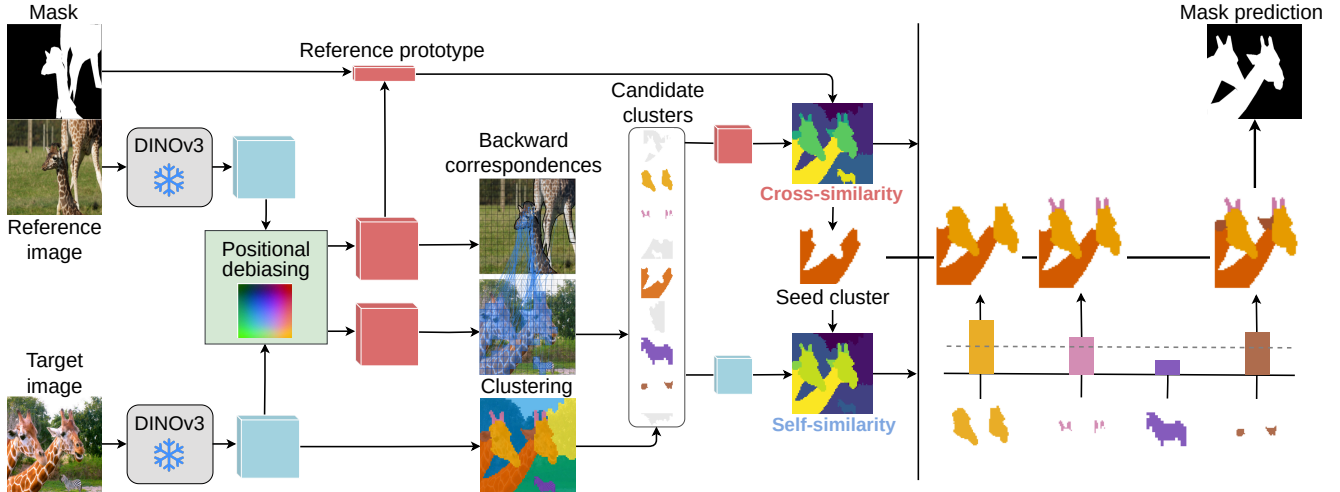


Figure 3. **Overview of INSID3.** We leverage the semantic and spatial structure of DINOv3 to perform in-context segmentation without training or model composition. Dense features from the reference and target images are first debiased to suppress positional bias, improving cross-image matching. The target is then decomposed into coherent regions through agglomerative clustering, providing a structured representation. We retain candidate clusters that match the reference through backward correspondence in the debiased space; a reference prototype derived from the annotated region anchors the *seed cluster* via cross-image similarity. Finally, we combine cross-image similarity, capturing semantic alignment, with self-similarity, measuring the affinity of each cluster to the seed, to form the final mask from the seed.

to ICS as a unified formulation of one-shot *semantic*, *part*, and *personalized* segmentation across different levels of semantic granularity within a single, general-purpose model.

Recent work follows two trends: *Training-free pipelines* [16, 39, 69] combine the semantic understanding of DINOv2 with segmentation priors from SAM, benefiting from strong generalization but inheriting SAM’s mask granularity and the computational burden of multi-stage designs. *Supervised methods* [41, 74] aim to unify both capabilities within a single VFM by injecting segmentation functionality via task-specific supervision. SegIC [41] trains a segmentation decoder on top of DINOv2, while DiffewS [74] fine-tunes Stable Diffusion [52]. Such training/fine-tuning couples the model to the training distribution, limiting its flexibility on unseen domains and granularities. In contrast, we address ICS with a single VFM *and* without training.

**Dense self-supervised representation learning (SSL)** aims to learn dense feature extractors from unlabeled data, enabling a broad range of vision tasks [15, 20]. Initial self-supervised approaches employ image-level pre-text tasks [5, 6, 8, 14, 19, 23, 35, 45], transferring suboptimally to pixel-level prediction [66, 67]. Later work aims to learn localized and discriminative dense features. Emergent properties in ViTs [7] can be uncovered through spatially local objectives [47, 73], spatio-temporal consistency [29], or spatial alignment across views [1, 46]. Localized supervision is also possible through contrastive objectives on region proposals [25, 26], or by predicting the cluster identity of masked tokens [13]. Moreover, SSL features can be refined *a-posteriori* [22, 65] or through limited fine-tuning [32, 53].

Recent efforts distill DINOv2 [47] together with weakly supervised VFMs, *e.g.*, SAM [33] or CLIP [49], to enhance spatial fidelity [2, 24, 51]. Most recently, DINOv3 [56] uses significant data and model scaling, a Gram anchoring objective, and high-resolution post-training to obtain an expressive, dense feature extractor. We show that dense DINOv3 features can be directly leveraged for in-context segmentation without fine-tuning or model composition.

### 3. In-context Segmentation with INSID3

Our goal is to segment arbitrary concepts, *i.e.*, objects, parts, or personalized instances, given an in-context example, using a frozen DINOv3 encoder without training or model composition. A key property of DINOv3 is the strong self-similarity of its dense features, naturally grouping coherent parts or objects (Fig. 2). However, in-context segmentation also requires establishing correspondences *across* images, which we find affected by a systematic *positional bias*: features from similar positions spuriously match across unrelated images. To address this, we propose a simple, training-free strategy to remove positional components from the features (Sec. 3.1). We use these *debiased features* for cross-image matching, while retaining the original features for intra-image similarity and clustering.

Our approach, named INSID3 and illustrated in Fig. 3, first partitions the target image into semantically coherent regions using self-similarity (Sec. 3.2). Then it identifies the cluster that is most semantically aligned with the reference region through cross-image similarity in the debiased space

(Sec. 3.3). Finally, it expands this seed region by aggregating clusters according to intra-image self-similarity, yielding a complete and coherent segmentation mask (Sec. 3.4).

**Task definition.** We let  $\mathbf{I}^r \in \mathbb{R}^{H \times W \times 3}$  denote the reference image with its binary mask  $\mathbf{M}^r \in \{0, 1\}^{H \times W}$ , and  $\mathbf{I}^t \in \mathbb{R}^{H \times W \times 3}$  a target image. We extract dense features from a frozen DINOv3 encoder  $\Phi(\cdot)$  [56]:

$$\mathbf{F}^r = \Phi(\mathbf{I}^r), \quad \mathbf{F}^t = \Phi(\mathbf{I}^t), \quad (1)$$

where  $\mathbf{F}^r, \mathbf{F}^t \in \mathbb{R}^{P \times D}$  denote the  $D$ -dimensional patch embeddings at resolution  $P = H' \times W'$ . We let  $\Omega = \{1, \dots, P\}$  denote the set of patch indices in  $\mathbf{F}^r$  and  $\mathbf{F}^t$ .

### 3.1. Unlocking the DINOv3 feature space

Solving the ICS task fundamentally relies on computing robust and reliable feature correspondences between the reference and target images [39]. As a diagnostic tool to evaluate DINOv3’s ability to establish reliable correspondences, we compute cross-image similarity to visualize how target patches align with the reference concept. Specifically, given the reference mask  $\mathbf{M}^r$  and the set of foreground patch indices<sup>1</sup>  $\mathcal{R} = \{j \in \Omega \mid \mathbf{M}_j^r = 1\}$ , we compute a reference prototype  $\mathbf{p}^r$  and its similarity to each target patch  $i \in \Omega$ :

$$\mathbf{p}^r = \frac{1}{|\mathcal{R}|} \sum_{j \in \mathcal{R}} \mathbf{F}_j^r, \quad \text{sim}(i) = \langle \mathbf{F}_i^t, \mathbf{p}^r \rangle. \quad (2)$$

This produces dense similarity maps, indicating how well each target patch aligns with the reference concept. We visualize these maps at two granularity levels: (i) at mask level (Fig. 4a), where the reference corresponds to an object, and (ii) at keypoint level (Fig. 4b), where the reference is a single annotated keypoint. The resulting similarity maps show that DINOv3 captures meaningful semantic correspondences between reference and target. However, they also exhibit a stable *positional bias*: features at a given position in the reference tend to produce spurious activations at the same position in the target, irrespective of semantics. These false activations typically occur where the target area lacks semantic content (e.g., uniform background regions), suggesting that positional information dominates weak semantic cues. To ground this intuition, Fig. 4c visualizes features from inputs with minimal semantic content: a principal component analysis (PCA) suggests a stable low-dimensional subspace associated with positional signals.

We use this signal as a simple and effective approximation of positional bias, which can be estimated once and removed consistently at inference time. Specifically, we estimate the positional subspace by passing a noise image  $\mathbf{I}^{\text{noise}} \sim \mathcal{N}(\mathbf{0}, \mathbf{1}) \in \mathbb{R}^{H \times W \times 3}$  through the encoder:

$$\mathbf{F}^{\text{noise}} = \Phi(\mathbf{I}^{\text{noise}}) \in \mathbb{R}^{P \times D}. \quad (3)$$

<sup>1</sup>In slight abuse of notation, we let  $\mathbf{M}_j^r$  denote the  $j^{\text{th}}$  patch of  $\mathbf{M}^r$ .

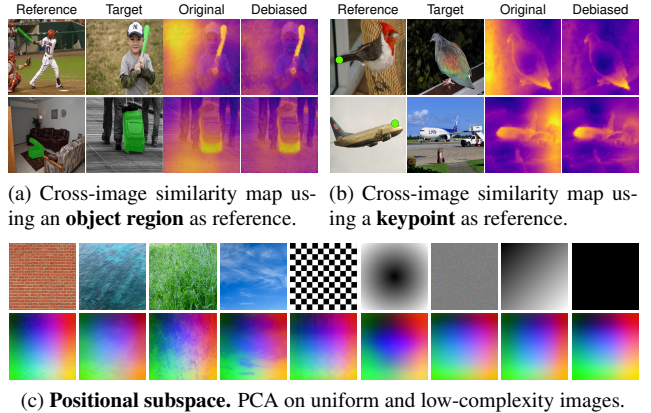


Figure 4. **Positional bias in DINOv3 features.** For both region (a) and keypoint (b) prompts, similarity maps computed with the original DINOv3 features show structured activations aligned with the reference coordinates, independent of semantics. Our debiased features mitigate this behavior. (c) PCA of features from images with low semantic complexity (e.g., noise, flat textures) reveals a stable low-dimensional positional subspace underlying this bias.

We apply singular value decomposition  $\mathbf{F}^{\text{noise}} = \mathbf{U}\Sigma\mathbf{V}^\top$  and select the top  $s$  right singular vectors  $\mathbf{B} = \mathbf{V}_{[:,1:s]}$  as a basis for the positional subspace. We then project both reference and target features onto its orthogonal complement:

$$\tilde{\mathbf{F}}^r = \mathbf{F}^r(\mathbf{1}_D - \mathbf{B}\mathbf{B}^\top) \quad \tilde{\mathbf{F}}^t = \mathbf{F}^t(\mathbf{1}_D - \mathbf{B}\mathbf{B}^\top). \quad (4)$$

The effect of this projection is to suppress positional components: using these debiased features to recompute the similarity map as in Eq. (2) yields activations that are less affected by structured positional bias (cf. Fig. 4). In the rest of the paper, we refer to  $\tilde{\mathbf{F}}^r, \tilde{\mathbf{F}}^t$  as *debiased features*.

Interestingly, this spatial dependency is markedly weaker in DINOv2; positional correlations are less pronounced and not as easily observable in similarity maps (cf. Supp. Material). We hypothesize this positional bias to be a by-product of the stronger local-consistency constraints in DINOv3. Namely, the *Gram anchoring* constrains the covariance matrix of patch embeddings, encouraging global statistics of features to remain stable throughout training. While improving spatial consistency, this objective may inadvertently amplify absolute spatial correlations, resulting in residual positional bias when semantic content is weak.

**Unlocked feature space.** We exploit the complementary nature of DINOv3 features by using: (i) our *debiased features* for cross-image semantic matching, where positional signals are harmful, and (ii) *original features* for intra-image grouping, where spatial structure is helpful.

### 3.2. Fine-grained clustering

The first step of our ICS pipeline is to partition the target image into semantically coherent regions. The dense feature maps of DINOv3 exhibit strong local consistency: As

shown by [56], patches belonging to the same object or part tend to have highly similar embeddings. We leverage this to group image regions in an unsupervised manner.

While  $K$ -means clustering has been widely used in self-supervised representation learning [6, 22, 40, 47], it requires predefining the number of clusters, which is ill-suited for the open-world nature and variable granularity of ICS. Density-based methods, *e.g.*, DBSCAN [17], struggle in high-dimensional feature spaces where the notion of density becomes unreliable [50, 55], and typically require dimensionality reduction. Instead, we adopt agglomerative clustering [43], which progressively merges locally similar features in a bottom-up manner, naturally aligning with the spatial smoothness of DINOv3. A single threshold hyperparameter  $\tau$  provides intuitive control over the resulting granularity without fixing a predefined number of regions.

Concretely, we partition the (original) target patch embeddings  $\mathbf{F}^t$  into  $K$  disjoint spatial regions via iterative agglomerative clustering, yielding clusters  $\{\mathcal{G}_1, \dots, \mathcal{G}_K\}$  such that

$$\bigcup_{k=1}^K \mathcal{G}_k = \Omega, \quad \mathcal{G}_i \cap \mathcal{G}_j = \emptyset \quad \forall i \neq j. \quad (5)$$

As shown in Fig. 2, this unsupervised approach produces spatially coherent clusters that provide a strong structural representation of the image.

### 3.3. Seed-cluster selection

Having partitioned the target image into semantically coherent regions, we identify the cluster that best corresponds to the reference region. We do this in two stages: *candidate localization* and *seed-cluster selection*.

**Candidate localization.** Directly correlating the reference prototype with all target patches, as in Fig. 4a, often produces broad activations on related concepts, even when the reference depicts only a specific part: *e.g.*, the prototype of a *person head* may trigger responses over the full person.

To adapt matching at the correct level of granularity, we instead compute *backward* correspondences, *i.e.* for each target patch  $i$ , we find its most similar reference patch  $j$ :

$$\text{NN}(i) = \arg \max_{j \in \Omega} \langle \tilde{\mathbf{F}}_i^t, \tilde{\mathbf{F}}_j^r \rangle, \quad (6)$$

Backward matching of target patches allows us to *implicitly leverage unannotated negatives* in the reference image. By retaining only target patches whose nearest neighbor in the reference falls within the support mask, we obtain a filtering mechanism that conservatively estimates the set  $\mathcal{C}_{\text{NN}}$  of target patches in which the reference concept may appear as

$$\mathcal{C}_{\text{NN}} = \{i \mid \mathbf{M}_{\text{NN}(i)}^r = 1\}. \quad (7)$$

Restricting the precomputed clusters  $\{\mathcal{G}_k\}$  to those that overlap with  $\mathcal{C}_{\text{NN}}$  yields the subset of candidate clusters

$$\mathcal{C}_{\text{cand}} = \{\mathcal{G}_k \mid \mathcal{G}_k \cap \mathcal{C}_{\text{NN}} \neq \emptyset\}. \quad (8)$$

**Seed selection.** We compute prototypes in the debiased feature space for both the candidate clusters  $\mathcal{G}_k \in \mathcal{C}_{\text{cand}}$  and the annotated reference region:

$$\tilde{\mathbf{p}}_k^t = \frac{1}{|\mathcal{G}_k|} \sum_{i \in \mathcal{G}_k} \tilde{\mathbf{F}}_i^t, \quad \tilde{\mathbf{p}}^r = \frac{1}{|\mathcal{R}|} \sum_{j \in \mathcal{R}} \tilde{\mathbf{F}}_j^r. \quad (9)$$

We then compute a cross-image similarity score

$$s_k^{\text{cross}} = \langle \tilde{\mathbf{p}}_k^t, \tilde{\mathbf{p}}^r \rangle, \quad (10)$$

measuring how well each candidate  $\mathcal{G}_k$  aligns semantically with the reference. The final seed cluster is selected as

$$\mathcal{G}^* = \arg \max_{\mathcal{G}_k \in \mathcal{C}_{\text{cand}}} s_k^{\text{cross}}, \quad (11)$$

corresponding to the target region that is most semantically aligned with the reference at the correct part granularity.

### 3.4. Cluster aggregation

The seed cluster  $\mathcal{G}^*$  provides a strong but typically *partial* localization of the semantic concept in the target, often covering only the most discriminative part of the concept, such as a person’s head or the neck of a giraffe (*cf.* Fig. 3). To recover the full extent of the concept, we evaluate all remaining candidate clusters to decide which should be merged. Intuitively, the cross-image similarity score  $s_k^{\text{cross}}$  (Eq. 10), reflects how semantically close candidate clusters  $\mathcal{G}_k$  are to the reference. However, relying solely on cross-image similarity can be unreliable under occlusions or viewpoint changes, where semantically relevant regions may appear dissimilar. Therefore, we propose to complement *semantic alignment* (across images) with *structural coherence* (within the target image). Specifically, we exploit a key property of DINOv3 [56]: *its features exhibit strong self-similarity within the same image*. Hence, clusters belonging to the same concept tend to lie close in feature space. For each candidate cluster, we thus compute its similarity to the seed in the *original* feature space as

$$\bar{\mathbf{p}}_k^t = \frac{1}{|\mathcal{G}_k|} \sum_{i \in \mathcal{G}_k} \mathbf{F}_i^t, \quad s_k^{\text{intra}} = \langle \bar{\mathbf{p}}_k^t, \bar{\mathbf{p}}_*^t \rangle, \quad (12)$$

where  $\bar{\mathbf{p}}_*^t$  denotes the prototype of the seed cluster  $\mathcal{G}^*$ .

**Final aggregation.** We combine semantic alignment and structural coherence through a multiplicative score, which favors clusters that are simultaneously semantically aligned with the reference and structurally consistent with the seed region. The final mask is obtained by merging the seed cluster with all candidate clusters whose combined score exceeds a similarity threshold  $\alpha$ :

$$S_k = s_k^{\text{cross}} \cdot s_k^{\text{intra}} \quad (13)$$

$$\mathcal{M}_{\text{final}} = \mathcal{G}^* \cup \{\mathcal{G}_k \in \mathcal{C}_{\text{cand}} \mid S_k \geq \alpha\}. \quad (14)$$

Table 1. Comparison of INSID3 (mIoU in %,  $\uparrow$ ) on one-shot semantic, part, and personalized segmentation. State-of-the-art methods are grouped into task-specific fine-tuning and training-free approaches. Previous training-free methods rely on SAM, pre-trained with mask-level supervision, whereas INSID3 uses only frozen self-supervised DINOv3 features. Gray indicates the model was trained on the corresponding train split of the dataset; best results **bold**, 2<sup>nd</sup> best underlined.  $\dagger$  denotes a GF-SAM variant using DINOv3 features.

Method	Encoder	#Param	Semantic						Part		Personalized	
			LVIS-92 <sup>i</sup>	COCO-20 <sup>i</sup>	ISIC	SUIM	iSAID	X-Ray	PASCAL	PACO	PerMIS	Avg
<b>Task-specific fine-tuning: <i>Semantic + mask supervision</i></b>												
Painter [63]	ViT	354 M	10.5	33.1	–	–	–	–	30.4	14.1	–	–
SegGPT [64]	ViT	354 M	18.6	56.1	37.5	34.9	30.9	<b>87.5</b>	35.8	13.5	18.7	37.1
SINE [38]	DINOv2	373 M	31.2	64.5	25.8	50.7	38.3	39.8	36.2	23.3	42.5	39.1
DiffewS [74]	Stable Diffusion	890 M	31.4	71.3	27.8	48.9	47.5	41.6	34.0	22.8	35.2	40.1
SegIC [41]	DINOv2	310 M	44.6	76.1	25.3	52.5	46.1	34.5	39.9	25.9	51.8	44.1
SegIC (coco) [41]	DINOv2	310 M	<u>35.7</u>	75.6	22.5	52.9	40.8	30.8	38.6	25.1	44.9	40.8
<b>Training free: <i>Mask-supervised pre-training</i></b>												
PerSAM [72]	SAM	640 M	11.5	23.0	23.9	28.7	19.2	31.7	32.5	22.5	48.6	26.8
Matcher [39]	DINOv2 + SAM	945 M	33.0	52.7	38.6	44.1	33.3	70.8	42.9	34.7	<u>63.8</u>	46.0
GF-SAM [69]	DINOv2 + SAM	945 M	35.2	<b>58.7</b>	48.7	<u>53.1</u>	47.1	51.0	44.5	<u>36.3</u>	54.1	47.6
GF-SAM <sup>†</sup> [69]	DINOv3 + SAM	945 M	31.8	54.8	50.9	50.5	46.7	56.1	44.9	34.4	52.6	47.0
$\hookrightarrow$ + our debias	DINOv3 + SAM	945 M	34.6	55.9	<u>51.8</u>	52.9	<u>47.6</u>	60.0	<u>46.2</u>	36.1	54.5	<u>48.8</u>
<b>Training free: <i>Unsupervised pre-training</i></b>												
<b>INSID3 (ours)</b>	DINOv3	<b>304 M</b>	<b>41.8</b>	<u>57.6</u>	<b>54.4</b>	<b>54.9</b>	<b>52.1</b>	<u>78.8</u>	<b>50.5</b>	<b>38.7</b>	<b>67.0</b>	<b>55.1</b>

## 4. Experiments

We evaluate INSID3 on one-shot *semantic*, *part*, and *personalized* segmentation. In each setting, a single annotated reference mask is provided, and the model is tasked with segmenting the corresponding concept in the target image: (1) *semantic* – all instances of a given class (e.g., “dog”); (2) *part* – same object part (e.g., “dog ear”); (3) *personalized* – same object instance (e.g., “my dog”).

For **one-shot semantic segmentation**, we use six datasets across a range of imaging scenarios: COCO-20<sup>i</sup> [44] with 80 object categories; LVIS-92<sup>i</sup> [39] with 920 categories and a strong long-tail distribution; ISIC2018 [10, 59] for skin lesion segmentation; Chest X-Ray [4, 30], an X-ray dataset of lung screening; iSAID-5<sup>i</sup> [68], a remote sensing dataset with 15 categories; and SUIM [28] with underwater imagery and 8 categories. For **one-shot part segmentation**, we use PASCAL-Part [39], providing 56 object parts across 15 categories, and PACO-Part [39] with 303 object parts from 75 categories. For **one-shot personalized segmentation**, we use PerMIS [54], covering 16 categories.

**Implementation details.** We adopt the Large version of the DINOv3 [56] encoder. Input images are resized to 1024  $\times$  1024, following SAM-based approaches [39, 69, 72]. The final segmentation masks are predicted at patch resolution: we bilinearly interpolate them to original resolution, and apply mask refinement with a CRF [36], following [21, 22, 40, 60]. We employ agglomerative clustering [43] with  $\tau = 0.6$  and set the cluster aggregation threshold to  $\alpha = 0.2$ . See Supplementary Material for more details.

### 4.1. Main results

**Baselines.** Table 1 compares against state-of-the-art ICS baselines in terms of mean Intersection-over-Union (mIoU). The primary baselines are *training-free methods*, specifically PerSAM [72], Matcher [39], and GF-SAM [69]. For GF-SAM, the strongest training-free baseline, we also include a variant in which DINOv2 is replaced with DINOv3 and a version with our feature debiasing to ensure a fair comparison. We also report *task-specific fine-tuning* methods such as SegIC [41] and DiffewS [74], which leverage semantic and mask supervision. For SegIC, we also report a version trained only on COCO. While these operate under a different supervision regime, they provide an upper reference point for in-domain accuracy. We emphasize that **INSID3** is the only method in Tab. 1 that uses no supervision (neither during pre-training nor fine-tuning) and operates solely on the self-supervised DINOv3 backbone.

**One-shot semantic segmentation.** Table 1 shows that INSID3 consistently outperforms training-free SAM-based pipelines, with gains over GF-SAM of +6.6 % pts. mIoU on LVIS-92<sup>i</sup>, +5.7 % pts. on ISIC, +1.8 % pts. on SUIM, and +27.8 % pts. on Chest X-ray, *etc.* Upgrading GF-SAM from DINOv2 to DINOv3 yields comparable performance, as its method relies only on sparse matched points to prompt SAM, thus discarding most of the information in DINOv3 dense features. However, our debiasing helps GF-SAM with DINOv3 ( pts. mIoU on average). In contrast, INSID3 performs estimation and segmentation in a unified space, achieving both higher accuracy and lower architec-

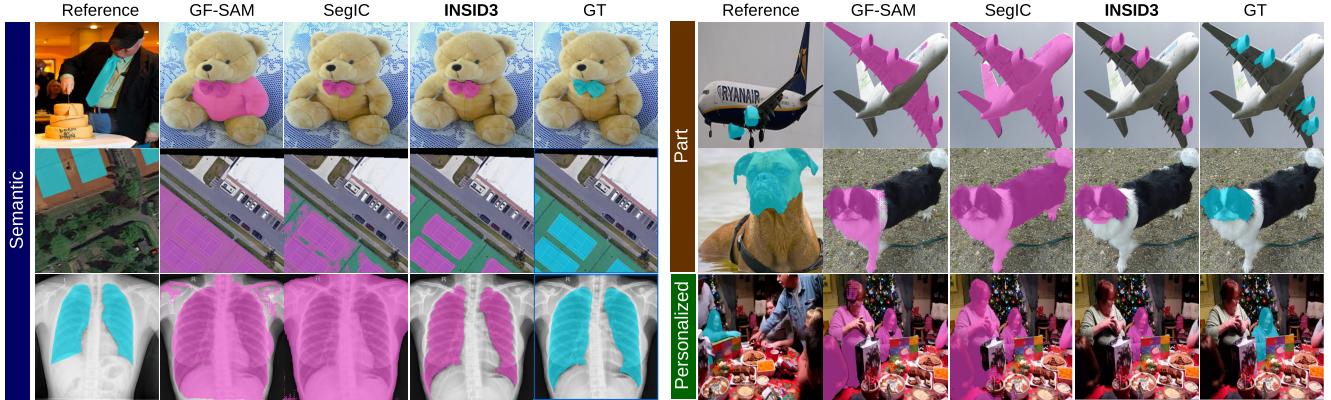


Figure 5. Comparison of **INSID3** with GF-SAM [69] and SegIC [41] on one-shot semantic (*left*), part (*top right*), and personalized (*bottom right*) segmentation. **SegIC** performs well in-domain but struggles to generalize across domains and part granularity, reflecting its limited flexibility beyond the training distribution. **GF-SAM**, relying on the strong segmentation priors of SAM [33], produces high-quality masks; however, the decoupled mechanism between correspondence and segmentation often leads to over- or under-segmentation. **INSID3**, despite relying solely on self-supervised features, achieves precise localization and competitive mask quality.

tural complexity (304 M vs. 945 M parameters). Interestingly, fine-tuned methods achieve strong in-domain results (e.g., SegIC reaches 76.1 % mIoU on COCO-20<sup>i</sup>) but drop sharply on other datasets, reflecting the inherent trade-off of specialization (e.g. -6 % w.r.t. INSID3 on iSAID). Qualitative results in Fig. 5 (*left*) show that INSID3 produces surprisingly clean segmentation masks directly from DINOv3 features, without any decoder or task-specific supervision.

**One-shot part segmentation.** INSID3 achieves significant improvements over existing baselines on also on part segmentation (*cf.* Tab. 1). It outperforms GF-SAM by +6.0 % pts. mIoU on PASCAL-Part and +2.4 % pts. mIoU on PACO-Part. Two-stage pipelines frequently over- or under-cover object parts due to fixed mask priors, inherited through fine-tuning or from SAM. In contrast, INSID3 better exploits the reference signal throughout the pipeline, enabling flexible and accurate part-level predictions. Compared to fine-tuned approaches, INSID3 outperforms SegIC and DiffewS by +10.6 % / +16.5 % pts. on PASCAL-Part and +12.8 % / +15.9 % pts. on PACO-Part. As illustrated in Fig. 5 (*top right*), INSID3 produces part masks that better preserve object structure and segmentation granularity.

**One-shot personalized segmentation.** INSID3 achieves the best results on PerMIS, reaching 67.0 % mIoU and surpassing GF-SAM by +12.9 % pts., SegIC by +15.2 % pts., and DiffewS by +31.8 % pts. This task is particularly challenging due to the presence of multiple visually similar distractor instances. Unlike previous work, which relies solely on positive activations from the reference and tends to segment all semantically related objects, INSID3 additionally exploits negative evidence through backward correspondences (Sec. 3.3) to suppress irrelevant regions. Figure 5 (*bottom right*) shows that this leads to accurate instance selection, even in the presence of visual ambiguity.

Table 2. **Semantic correspondence on SPair-71k** (PCK@ $T$  in %,  $\uparrow$ ). Comparison across DINOv3 backbones, w/ and w/o debiasing.

$T$	Small		Base		Large	
	<i>original</i>	<i>debias</i>	<i>original</i>	<i>debias</i>	<i>original</i>	<i>debias</i>
<b>0.05</b>	26.8	<b>27.9</b>	29.2	<b>32.3</b>	32.7	<b>33.6</b>
<b>0.10</b>	43.8	<b>45.7</b>	45.0	<b>50.0</b>	50.6	<b>52.0</b>
<b>0.15</b>	53.2	<b>55.6</b>	54.0	<b>59.9</b>	60.3	<b>62.1</b>
<b>0.20</b>	59.8	<b>62.6</b>	59.8	<b>66.4</b>	66.4	<b>68.6</b>

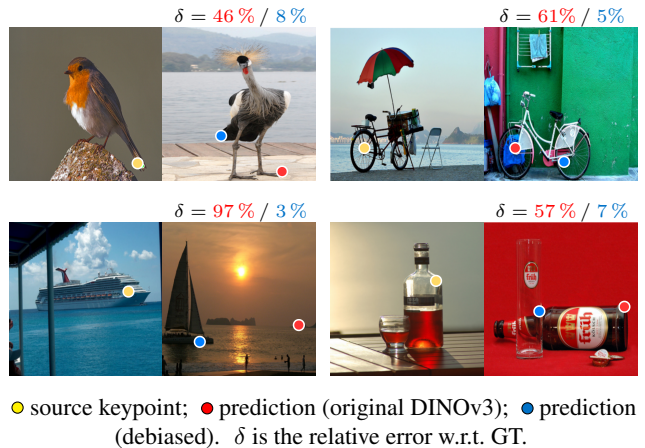


Figure 6. **Qualitative examples on SPair-71k** with DINOv3-L.

## 4.2. On the positional bias of DINOv3 features

While we focus on ICS, the positional bias we uncover in DINOv3 has broader implications for tasks that rely on semantic image alignment without spatial priors. A representative example is *semantic correspondence* [57, 70, 71], which evaluates how well dense features can localize semantically corresponding points across different images. We evaluate our debiasing strategy on SPair-71k [42], the

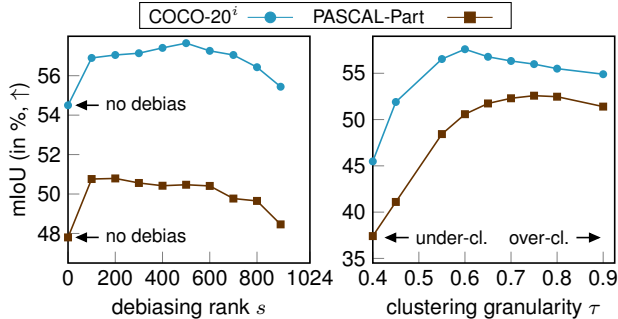


Figure 7. **INSID3 hyperparameters.** We study the effect of the debiasing rank  $s$  (left) and the clustering granularity  $\tau$  (right) on semantic (COCO-20<sup>i</sup>) and part (PASCAL-Part) segmentation.

standard benchmark for this task. Following common evaluation protocol [57, 70], for each source keypoint, we compute cosine similarity to all target patch tokens and select the most similar one. Accuracy is measured using PCK@ $T$  (% of Correct Keypoints within a normalized distance  $T$ ).

Quantitatively, Tab. 2 shows that debiasing leads to consistent gains of +0.9–6.6 PCK across all model sizes. These results show that our positional debiasing acts as a simple training-free correction that improves the reliability of DINOv3 features for tasks requiring semantic alignment across images. Qualitatively, Fig. 6 compares predictions obtained with the original DINOv3 features (*red*) and our debiased features (*blue*). Predictions based on original features are influenced by a mix of semantic and positional cues, resulting in systematic errors. In contrast, debiased features align closely with the correct semantic location, yielding more semantically grounded matches.

### 4.3. Ablation study

We conduct ablations on COCO-20<sup>i</sup> and PASCAL-Part. For more analyses, please refer to the Supplementary Material.

**Debiased feature space.** We study the influence of the rank  $s$  of the estimated positional subspace  $\mathbf{B}$  on our proposed *debiasing* of DINOv3 from Eq. (4). Fig. 7 (left) shows a stable trend, improving over the *no debiasing* baseline (*i.e.*,  $s = 0$ ), indicating that the removed positional subspace does not carry semantically meaningful information. Beyond an intermediate range, the gain saturates and eventually reverses once too many subspace dimensions are being removed. We fix  $s$  to 500 across all datasets, which yields consistent gains (+3.1 % on COCO, +2.7 % on PASCAL and up to +6.6 % PCK on SPair-71k, *cf.* Tab. 2).

**Cluster granularity.** Next, we analyze the impact of the *similarity threshold*  $\tau$  of agglomerative clustering (Sec. 3.2). Fig. 7 (right) shows that finer partitions resulting from larger  $\tau$  are beneficial for part-level tasks. Conversely, over-clustering is detrimental to object-level tasks, fragmenting coherent objects into many small clusters. We

Table 3. **Effect of clustering and aggregation.** We compare our approach with tuned baselines on COCO-20<sup>i</sup> and PASCAL-Part (mIoU %,  $\uparrow$ ). All thresholds (0.55) and clustering granularities ( $\tau=0.5$ ,  $\tau=0.6$ ) are tuned to optimal values for fair comparison.

Variant	COCO	PASCAL-Part
<i>No clustering</i>		
Thresholding sim. map @ 0.55 (Eq. 2)	44.2	35.4
<i>Clustering w/o aggregation</i>		
Coarse clustering ( $\tau = 0.5$ )	50.6	31.1
Fine clustering ( $\tau = 0.6$ )	42.8	36.2
<b>Ours: Clustering w/ aggregation (<math>\tau = 0.6</math>)</b>		
w/ cross similarity	54.6	48.5
w/ self + cross similarity (Eq. 13)	<b>57.6</b>	<b>50.5</b>

set  $\tau = 0.6$  across tasks, providing a sensible trade-off between part sensitivity and semantic coherence.

**Clustering and aggregation.** We lastly analyze the role of clustering and aggregation in Tab. 3. Thresholding the similarity map (Eq. 2) provides a coarse baseline, yielding 44.2 % and 35.4 % mIoU on COCO and PASCAL-Part. Introducing clustering without aggregation, where a single cluster is selected, improves results but requires tuning the granularity parameter  $\tau$  separately for each task: lower values ( $\tau = 0.5$ ) better capture full objects, while higher ones ( $\tau = 0.6$ ) suit part-level structures. Even tuned independently, this variant still underperforms. Our solution fixes an intermediate  $\tau$  and resolves this trade-off through a principled aggregation strategy (*cf.* Sec. 3.4). Aggregating by cross-image similarity already improves segmentation results, achieving 54.6 % and 48.5 %, while jointly leveraging cross- and self-similarity yields the best results, reaching 57.6 % and 50.5 % mIoU on COCO and PASCAL-Part.

## 5. Conclusion

In this work, we introduced INSID3, a training-free framework for in-context segmentation built solely on DINOv3. By leveraging the dual nature of DINOv3 features, *i.e.* semantic alignment and spatial coherence, INSID3 performs correspondence estimation and segmentation within a single backbone. Despite its simplicity, it exhibits strong generalization across one-shot *semantic*, *part*, and *personalized segmentation*, outperforming both fine-tuned and training-free approaches. Overall, this suggests that segmentation can emerge naturally from self-supervised dense representations. While existing methods rely on either fine-tuning or training-free pipelines grounded in mask-supervised pre-training, INSID3 remains fully *unsupervised*, relying solely on the in-context example for guidance. This suggests that reducing supervision may foster more robust and transferable representations, marking a concrete step toward more scalable and general-purpose visual understanding.

**Acknowledgments.** Claudia Cuttano was supported by the Sustainable Mobility Center (CNMS), which received funding from the European Union Next Generation EU (Piano Nazionale di Ripresa e Resilienza (PNRR), Missione 4 Componente 2 Investimento 1.4 “Potenziamento strutture di ricerca e creazione di ‘campioni nazionali di R&S’ su alcune Key Enabling Technologies”) with grant agreement no. CN\_00000023. Christoph Reich is supported by the Konrad Zuse School of Excellence in Learning and Intelligent Systems (ELIZA) through the DAAD programme Konrad Zuse Schools of Excellence in Artificial Intelligence, sponsored by the German Federal Ministry of Education and Research. Stefan Roth has received funding from the European Research Council (ERC) under the European Union’s Horizon 2020 research and innovation programme (grant agreement No. 866008). Further, he was supported by the DFG under Germany’s Excellence Strategy (EXC-3057/1 “Reasonable Artificial Intelligence”, Project No. 533677015) and by the LOEWE initiative (Hesse, Germany) within the emergenCITY center [LOEWE/1/12/519/03/05.001(0016)/72]. Daniel Cremers has received funding by the European Research Council (ERC) Advanced Grant SIMULACRON (grant agreement No. 884679). We acknowledge the CINECA award under the ISCRA initiative, for the availability of high-performance computing resources. We also acknowledge the support of the European Laboratory for Learning and Intelligent Systems (ELLIS). Finally, we thank Barış Zöngür for the insightful feedback.

## References

- [1] Adrien Bardes, Jean Ponce, and Yann LeCun. VICRegL: Self-supervised learning of local visual features. In *NeurIPS*, pages 8799–8810, 2022. 3
- [2] Daniel Bolya, Po-Yao Huang, Peize Sun, Jang Hyun Cho, Andrea Madotto, Chen Wei, Tengyu Ma, Jiale Zhi, Jathushan Rajasegaran, Hanoona Rasheed, et al. Perception Encoder: The best visual embeddings are not at the output of the network. In *NeurIPS*, 2025. 3, v
- [3] Tom Brown, Benjamin Mann, Nick Ryder, Melanie Subbiah, Jared D. Kaplan, Prafulla Dhariwal, Arvind Neelakantan, Pranav Shyam, Girish Sastry, Amanda Askell, et al. Language models are few-shot learners. In *NeurIPS*, pages 1877–1901, 2020. 1, 2
- [4] Sema Candemir, Stefan Jaeger, Kannappan Palaniappan, Jonathan P. Musco, Rahul K. Singh, Zhiyun Xue, Alexandros Karagyris, Sameer Antani, George Thoma, and Clement J. McDonald. Lung segmentation in chest radiographs using anatomical atlases with nonrigid registration. *IEEE Trans. Med. Imaging*, 33(2):577–590, 2013. 6
- [5] Mathilde Caron, Piotr Bojanowski, Armand Joulin, and Matthijs Douze. Deep clustering for unsupervised learning of visual features. In *ECCV*, volume 14, pages 132–149, 2018. 3
- [6] Mathilde Caron, Ishan Misra, Julien Mairal, Priya Goyal, Piotr Bojanowski, and Armand Joulin. Unsupervised learning of visual features by contrasting cluster assignments. In *NeurIPS*, pages 9912–9924, 2020. 3, 5
- [7] Mathilde Caron, Hugo Touvron, Ishan Misra, Hervé Jégou, Julien Mairal, Piotr Bojanowski, and Armand Joulin. Emerging properties in self-supervised vision transformers. In *ICCV*, pages 9650–9660, 2021. 2, 3
- [8] Ting Chen, Simon Kornblith, Mohammad Norouzi, and Geoffrey Hinton. A simple framework for contrastive learning of visual representations. In *ICML*, pages 1597–1607, 2020. 3
- [9] Aakanksha Chowdhery, Sharan Narang, Jacob Devlin, Maarten Bosma, Gaurav Mishra, Adam Roberts, Paul Barham, Hyung Won Chung, Charles Sutton, Sebastian Gehrmann, Parker Schuh, Kensen Shi, et al. PaLM: Scaling language modeling with pathways. *J. Mach. Learn. Res.*, 24(240):1–113, 2023. 1, 2
- [10] Noel Codella, Veronica Rotemberg, Philipp Tschandl, M. Emre Celebi, Stephen Dusza, David Gutman, Brian Helba, Aadi Kalloo, Konstantinos Liopyris, Michael Marchetti, Harald Kittler, and Allan Halpern. Skin lesion analysis toward melanoma detection 2018: A challenge hosted by the international skin imaging collaboration (ISIC). *arXiv:1902.03368 [cs.CV]*, 2019. 6
- [11] Marius Cordts, Mohamed Omran, Sebastian Ramos, Timo Rehfeld, Markus Enzweiler, Rodrigo Benenson, Uwe Franke, Stefan Roth, and Bernt Schiele. The Cityscapes dataset for semantic urban scene understanding. In *CVPR*, pages 3213–3223, 2016. 1
- [12] Claudia Cuttano, Gabriele Trivigno, Giuseppe Averta, and Carlo Masone. SANSA: Unleashing the hidden semantics in SAM2 for few-shot segmentation. In *NeurIPS*, 2025. 2, v
- [13] Timothée Darcet, Federico Baldassarre, Maxime Oquab, Julien Mairal, and Piotr Bojanowski. Cluster and predict latents patches for improved masked image modeling. *Trans. Mach. Learn. Res.*, 2025. 3
- [14] Carl Doersch, Abhinav Gupta, and Alexei A. Efros. Unsupervised visual representation learning by context prediction. In *ICCV*, pages 1422–1430, 2015. 3
- [15] Linus Ericsson, Henry Gouk, and Timothy M. Hospedales. How well do self-supervised models transfer? In *CVPR*, pages 5414–5423, 2021. 3
- [16] Miguel Espinosa, Chenhongyi Yang, Linus Ericsson, Steven McDonagh, and Elliot J. Crowley. No time to train! Training-free reference-based instance segmentation. *arXiv:2507.01300 [cs.CV]*, 2025. 3
- [17] Martin Ester, Hans-Peter Kriegel, Jörg Sander, and Xiaowei Xu. A density-based algorithm for discovering clusters in large spatial databases with noise. In *KDD*, pages 226–231, 1996. 5
- [18] Andreas Geiger, Philip Lenz, Christoph Stiller, and Raquel Urtasun. Vision meets robotics: The KITTI dataset. *Int. J. Robot. Res.*, 32(11):1231–1237, 2013. 1
- [19] Jean-Bastien Grill, Florian Strub, Florent Altché, Corentin Tallec, Pierre Richemond, Elena Buchatskaya, Carl Doersch, Bernardo Avila Pires, Zhaohan Guo, Mohammad Gheshlaghi Azar, Bilal Piot, Koray Kavukcuoglu, Munos Rémi, and Valco Michal. Bootstrap your own latent: A new approach to self-supervised learning. In *NeurIPS*, pages 21271–21284, 2020. 3

- [20] Jie Gui, Tuo Chen, Jing Zhang, Qiong Cao, Zhenan Sun, Hao Luo, and Dacheng Tao. A survey on self-supervised learning: Algorithms, applications, and future trends. *IEEE Trans. Pattern Anal. Mach. Intell.*, 46(12):9052–9071, 2024. 3
- [21] Oliver Hahn, Christoph Reich, Nikita Araslanov, Daniel Cremers, Christian Rupprecht, and Stefan Roth. Scene-centric unsupervised panoptic segmentation. In *CVPR*, pages 24485–24495, 2025. 6
- [22] Mark Hamilton, Zhoutong Zhang, Bharath Hariharan, Noah Snavely, and William T. Freeman. Unsupervised semantic segmentation by distilling feature correspondences. In *ICLR*, 2022. 3, 5, 6
- [23] Kaiming He, Haoqi Fan, Yuxin Wu, Saining Xie, and Ross Girshick. Momentum contrast for unsupervised visual representation learning. In *CVPR*, pages 9729–9738, 2020. 3
- [24] Greg Heinrich, Mike Ranzinger, Hongxu, Yin, Yao Lu, Jan Kautz, Andrew Tao, Bryan Catanzaro, and Pavlo Molchanov. RADIOv2.5: Improved baselines for agglomerative vision foundation models. In *CVPR*, pages 22487–22497, 2025. 3
- [25] Olivier J. Hénaff, Skanda Koppula, Jean-Baptiste Alayrac, Aaron Van den Oord, Oriol Vinyals, and João Carreira. Efficient visual pretraining with contrastive detection. In *ICCV*, pages 10086–10096, 2021. 3
- [26] Olivier J. Hénaff, Skanda Koppula, Evan Shelhamer, Daniel Zoran, Andrew Jaegle, Andrew Zisserman, João Carreira, and Relja Arandjelović. Object discovery and representation networks. In *ECCV*, volume 27, pages 123–143, 2022. 3
- [27] Sunghwan Hong, Seokju Cho, Jisu Nam, Stephen Lin, and Seungryong Kim. Cost aggregation with 4D convolutional Swin transformer for few-shot segmentation. In *ECCV*, pages 108–126, 2022. 2
- [28] Md Jahidul Islam, Chelsey Edge, Yuyang Xiao, Peigen Luo, Muntaqim Mehtaz, Christopher Morse, Sadman Sakib Enan, and Junaed Sattar. Semantic segmentation of underwater imagery: Dataset and benchmark. In *IROS*, pages 1769–1776, 2020. 6
- [29] Allan Jabri, Andrew Owens, and Alexei Efros. Space-time correspondence as a contrastive random walk. In *NeurIPS*, pages 19545–19560, 2020. 3
- [30] Stefan Jaeger, Alexandros Karargyris, Sema Candemir, Les Folio, Jenifer Siegelman, Fiona Callaghan, Zhiyun Xue, Kannappan Palaniappan, Rahul K. Singh, Sameer Antani, et al. Automatic tuberculosis screening using chest radiographs. *IEEE Trans. Med. Imaging*, 33(2):233–245, 2013. 6
- [31] Joel Janai, Fatma Güneş, Aseem Behl, and Andreas Geiger. Computer vision for autonomous vehicles: Problems, datasets and state of the art. *Found. Trends Comput. Graph. Vis.*, 12(1–3):1–308, 2020. 1
- [32] Aleksandar Jevtić, Christoph Reich, Felix Wimbauer, Oliver Hahn, Christian Rupprecht, Stefan Roth, and Daniel Cremers. Feed-forward SceneDINO for unsupervised semantic scene completion. In *ICCV*, pages 6784–6796, 2025. 3, iii
- [33] Alexander Kirillov, Eric Mintun, Nikhila Ravi, Hanzi Mao, Chloe Rolland, Laura Gustafson, Tete Xiao, Spencer Whitehead, Alexander C. Berg, Wan-Yen Lo, Piotr Dollar, and Ross Girshick. Segment Anything. In *ICCV*, pages 4015–4026, 2023. 2, 3, 7
- [34] Tae-young Ko and Seung-ho Lee. Novel method of semantic segmentation applicable to augmented reality. *Sensors*, 20(6):1737, 2020. 1
- [35] Nikos Komodakis and Spyros Gidaris. Unsupervised representation learning by predicting image rotations. In *ICLR*, 2018. 3
- [36] Philipp Krähenbühl and Vladlen Koltun. Efficient inference in fully connected CRFs with Gaussian edge potentials. In *NIPS*, pages 109–117, 2011. 6
- [37] Chunbo Lang, Gong Cheng, Binfei Tu, and Junwei Han. Learning what not to segment: A new perspective on few-shot segmentation. In *CVPR*, pages 8057–8067, 2022. 2
- [38] Yang Liu, Chenchen Jing, Hengtao Li, Muzhi Zhu, Hao Chen, Xinlong Wang, and Chunhua Shen. A simple image segmentation framework via in-context examples. In *NeurIPS*, pages 25095–25119, 2024. 1, 6, iv
- [39] Yang Liu, Muzhi Zhu, Hengtao Li, Hao Chen, Xinlong Wang, and Chunhua Shen. Matcher: Segment anything with one shot using all-purpose feature matching. In *ICLR*, 2024. 1, 2, 3, 4, 6, iv, v, vi
- [40] Luke Melas-Kyriazi, Christian Rupprecht, Iro Laina, and Andrea Vedaldi. Deep spectral methods: A surprisingly strong baseline for unsupervised semantic segmentation and localization. In *CVPR*, pages 8364–8375, 2022. 5, 6
- [41] Lingchen Meng, Shiyi Lan, Hengduo Li, Jose M. Alvarez, Zuxuan Wu, and Yu-Gang Jiang. SegIC: Unleashing the emergent correspondence for in-context segmentation. In *ECCV*, volume 38, pages 203–220, 2024. 1, 3, 6, 7, v, vi
- [42] Juhong Min, Jongmin Lee, Jean Ponce, and Minsu Cho. SPair-71k: A large-scale benchmark for semantic correspondence. *arXiv:1908.10543 [cs.CV]*, 2019. 7, ii
- [43] Daniel Müllner. Modern hierarchical, agglomerative clustering algorithms. *arXiv:1109.2378 [stat.ML]*, 2011. 5, 6
- [44] Khoi Nguyen and Sinisa Todorovic. Feature weighting and boosting for few-shot segmentation. In *ICCV*, pages 622–631, 2019. 6
- [45] Mehdi Noroozi and Paolo Favaro. Unsupervised learning of visual representations by solving jigsaw puzzles. In *ECCV*, volume 6, pages 69–84, 2016. 3
- [46] Pedro O. Pinheiro, Amjad Almahairi, Ryan Benmalek, Florian Golemo, and Aaron C. Courville. Unsupervised learning of dense visual representations. In *NeurIPS*, pages 4489–4500, 2020. 3
- [47] Maxime Oquab, Timothée Darcet, Théo Moutakanni, Huy Vo, Marc Szafraniec, Vasil Khalidov, Pierre Fernandez, Daniel Haziza, Francisco Massa, Alaaeldin El-Nouby, et al. DINOv2: Learning robust visual features without supervision. *Trans. Mach. Learn. Res.*, 2024. 1, 2, 3, 5, i, v
- [48] Long Ouyang, Jeffrey Wu, Xu Jiang, Diogo Almeida, Carroll Wainwright, Pamela Mishkin, Chong Zhang, Sandhini Agarwal, Katarina Slama, Alex Ray, et al. Training language models to follow instructions with human feedback. In *NeurIPS*, pages 27730–27744, 2023. 1, 2
- [49] Alec Radford, Jong Wook Kim, Chris Hallacy, Aditya Ramesh, Gabriel Goh, Sandhini Agarwal, Girish Sastry,

- Amanda Askill, Pamela Mishkin, Jack Clark, et al. Learning transferable visual models from natural language supervision. In *ICML*, pages 8748–8763, 2021. 3
- [50] Miloš Radovanovic, Alexandros Nanopoulos, and Mirjana Ivanovic. Hubs in space: Popular nearest neighbors in high-dimensional data. *J. Mach. Learn. Res.*, 11(86):2487–2531, 2010. 5
- [51] Mike Ranzinger, Greg Heinrich, Jan Kautz, and Pavlo Molchanov. AM-RADIO: Agglomerative vision foundation model reduce all domains into one. In *CVPR*, pages 12490–12500, 2024. 3
- [52] Robin Rombach, Andreas Blattmann, Dominik Lorenz, Patrick Esser, and Björn Ommer. High-resolution image synthesis with latent diffusion models. In *CVPR*, pages 10684–10695, 2022. 1, 3, v
- [53] Mohammadreza Salehi, Efstratios Gavves, Cees G.M. Snoek, and Yuki M. Asano. Time does tell: Self-supervised time-tuning of dense image representations. In *ICCV*, pages 16536–16547, 2023. 3
- [54] Dvir Samuel, Rami Ben-Ari, Matan Levy, Nir Darshan, and Gal Chechik. Where’s Waldo: Diffusion features for personalized segmentation and retrieval. In *NeurIPS*, pages 128160–128181, 2024. 6
- [55] Erich Schubert, Jörg Sander, Martin Ester, Hans Peter Kriegel, and Xiaowei Xu. DBSCAN revisited, revisited: Why and how you should (still) use DBSCAN. *ACM Trans. Database Syst.*, 42(3), 2017. 5
- [56] Oriane Siméoni, Huy V. Vo, Maximilian Seitzer, Federico Baldassarre, Maxime Oquab, Cijo Jose, Vasil Khalidov, Marc Szafraniec, Seungeun Yi, Michaël Ramamonjisoa, et al. DINOv3. *arXiv:2508.10104 [cs.CV]*, 2025. 1, 2, 3, 4, 5, 6, i
- [57] Luming Tang, Menglin Jia, Qianqian Wang, Cheng Perng Phoo, and Bharath Hariharan. Emergent correspondence from image diffusion. In *NeurIPS*, pages 1363–1389, 2023. 1, 7, 8
- [58] Hugo Touvron, Thibaut Lavril, Gautier Izacard, Xavier Martinet, Marie-Anne Lachaux, Timothée Lacroix, Baptiste Rozière, Naman Goyal, Eric Hambro, Faisal Azhar, et al. LLaMA: Open and Efficient Foundation Language Models. *arXiv:2302.13971 [cs.CV]*, 2023. 1, 2
- [59] Philipp Tschandl, Cliff Rosendahl, and Harald Kittler. The HAM10000 dataset, a large collection of multi-source dermatoscopic images of common pigmented skin lesions. *Sci. Data*, 5(1):1–9, 2018. 6
- [60] Wouter Van Gansbeke, Simon Vandenhende, Stamatios Georgoulis, and Luc Van Gool. Unsupervised semantic segmentation by contrasting object mask proposals. In *ICCV*, pages 10052–10062, 2021. 6
- [61] Kaixin Wang, Jun Hao Liew, Yingtian Zou, Daquan Zhou, and Jiashi Feng. PaNet: Few-shot image semantic segmentation with prototype alignment. In *ICCV*, pages 9197–9206, 2019. 2
- [62] Risheng Wang, Tao Lei, Ruixia Cui, Bingtao Zhang, Hongying Meng, and Asoke K. Nandi. Medical image segmentation using deep learning: A survey. *IET Image Process.*, 16(5): 1243–1267, 2022. 1
- [63] Xinlong Wang, Wen Wang, Yue Cao, Chunhua Shen, and Tiejun Huang. Images speak in images: A generalist painter for in-context visual learning. In *CVPR*, pages 6830–6839, 2023. 2, 6
- [64] Xinlong Wang, Xiaosong Zhang, Yue Cao, Wen Wang, Chunhua Shen, and Tiejun Huang. SegGPT: Towards segmenting everything in context. In *ICCV*, pages 1130–1140, 2023. 2, 6, iv, vi
- [65] Monika Wysoczańska, Oriane Siméoni, Michaël Ramamonjisoa, Andrei Bursuc, Tomasz Trzcíński, and Patrick Pérez. CLIP-DINOiser: Teaching CLIP a few DINO tricks for open-vocabulary semantic segmentation. In *ECCV*, volume 61, pages 320–337, 2024. 3
- [66] Ceyuan Yang, Zhirong Wu, Bolei Zhou, and Stephen Lin. Instance localization for self-supervised detection pretraining. In *CVPR*, pages 3987–3996, 2021. 3
- [67] Junwei Yang, Ke Zhang, Zhaolin Cui, Jinming Su, Junfeng Luo, and Xiaolin Wei. InsCon: Instance consistency feature representation via self-supervised learning. *arXiv:2203.07688 [cs.CV]*, 2022. 3
- [68] Xiwen Yao, Qinglong Cao, Xiaoxu Feng, Gong Cheng, and Junwei Han. Scale-aware detailed matching for few-shot aerial image semantic segmentation. *IEEE Trans. Geosci. Remote. Sens.*, 60:1–11, 2021. 6
- [69] Anqi Zhang, Guangyu Gao, Jianbo Jiao, Chi Harold Liu, and Yunchao Wei. Bridge the points: Graph-based few-shot segment anything semantically. In *NeurIPS*, pages 33232–33261, 2024. 2, 3, 6, 7, iv, v, vi
- [70] Junyi Zhang, Charles Herrmann, Junhwa Hur, Luisa Polania Cabrera, Varun Jampani, Deqing Sun, and Ming-Hsuan Yang. A tale of two features: Stable Diffusion complements DINO for zero-shot semantic correspondence. In *NeurIPS*, pages 45533–45547, 2023. 1, 7, 8
- [71] Junyi Zhang, Charles Herrmann, Junhwa Hur, Eric Chen, Varun Jampani, Deqing Sun, and Ming-Hsuan Yang. Telling left from right: Identifying geometry-aware semantic correspondence. In *CVPR*, pages 3076–3085, 2024. 7
- [72] Renrui Zhang, Zhengkai Jiang, Ziyu Guo, Shilin Yan, Junting Pan, Xianzheng Ma, Hao Dong, Peng Gao, and Hongsheng Li. Personalize segment anything model with one shot. In *ICLR*, 2024. 1, 2, 6, vi
- [73] Jinghao Zhou, Chen Wei, Huiyu Wang, Wei Shen, Cihang Xie, Alan Yuille, and Tao Kong. iBOT: Image BERT pre-training with online tokenizer. In *ICLR*, 2022. 3
- [74] Muzhi Zhu, Yang Liu, Zekai Luo, Chenchen Jing, Hao Chen, Guangkai Xu, Xinlong Wang, and Chunhua Shen. Unleashing the potential of the diffusion model in few-shot semantic segmentation. In *NeurIPS*, pages 42672–42695, 2024. 1, 3, 6, iv, v

# INSID3: Training-Free In-Context Segmentation with DINOv3

## Supplementary Material

Claudia Cattano\*<sup>1,2</sup>

Gabriele Trivigno\*<sup>1</sup>

Christoph Reich<sup>2,3,5,6</sup>

Daniel Cremers<sup>3,5,6</sup>

Carlo Masone<sup>1</sup>

Stefan Roth<sup>2,4,5</sup>

<sup>1</sup>Politecnico di Torino

<sup>2</sup>TU Darmstadt

<sup>3</sup>TU Munich

<sup>4</sup>hessian.AI

<sup>5</sup>ELIZA

<sup>6</sup>MCML

\*equal contribution

<https://visinf.github.io/INSID3>

In this appendix, we provide additional analyses, implementation details, and experiments for INSID3.

Specifically:

- **Positional bias.** In Sec. A, we further analyze the issue of positional bias in DINOv3, including comparisons with DINOv2 and additional debiasing studies.
- **Implementation details.** In Sec. B, we report the hyperparameters used throughout the paper. The same set of hyperparameters is fixed across all datasets and tasks.
- **Additional experiments.** In Sec. C, we present further experiments, including the 5-shot setting, backbone comparisons, evaluation against SAM 3, and the empty-mask corner case.
- **Computational cost.** In Sec. D, we analyze the computational cost of our method and compare it against training-free and fine-tuned baselines.
- **Qualitative examples.** In Sec. E, we report additional qualitative comparisons and examples of our method.
- **Limitations and future directions.** In Sec. F, we discuss current limitations of INSID3 and outline possible extensions.

## A. On the Positional Bias

### A.1. DINOv2 vs. DINOv3: Positional bias

To assess how strongly positional bias is encoded in DINOv3 [56] versus DINOv2 [47], we analyze the similarity maps from both encoders, computed as in Sec. 3.1 of the main paper. Given a reference image with one annotated keypoint and a target image, we extract dense patch embeddings  $\mathbf{F}^r$  and  $\mathbf{F}^t$  from the respective backbone, let  $j$  denote the patch index of the keypoint, and form the reference prototype

$$\mathbf{p}^r = \mathbf{F}_j^r. \quad (15)$$

We then compute the target similarity map as

$$\text{sim}(i) = \langle \mathbf{F}_i^t, \mathbf{p}^r \rangle, \quad i \in \{1, 2, \dots, P\}. \quad (16)$$

For each backbone, we visualize (i) the similarity map obtained from the original features, and (ii) the similarity map obtained after applying our debiasing projection from Eqs. (3) and (4) from the main paper. These similarities are visualized in Fig. 8. The maps show a notable difference between the two models. With the original *DINOv3* features, we observe pronounced coordinate-

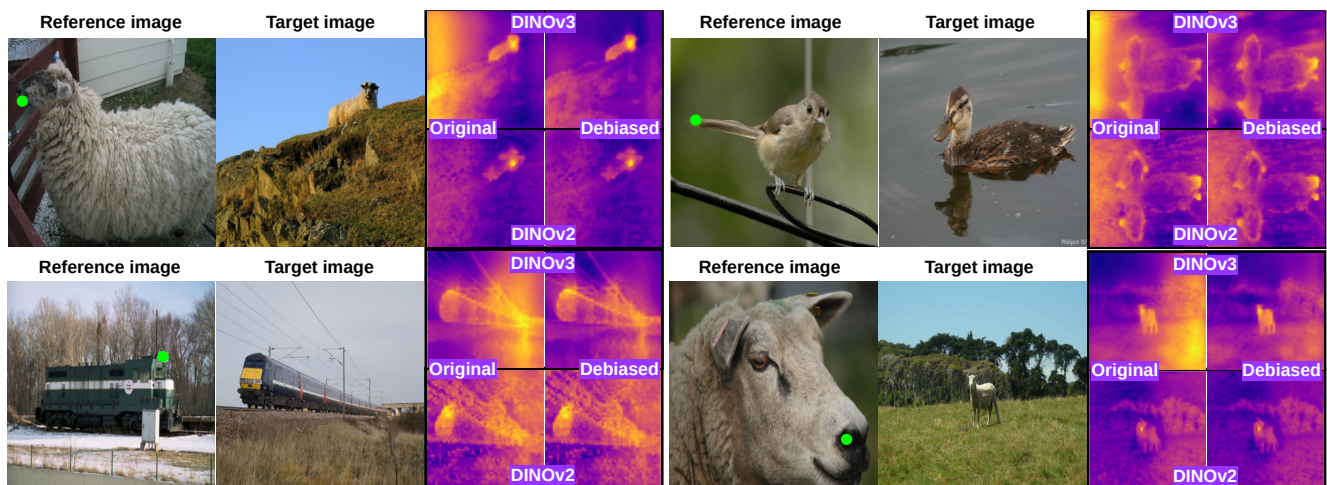


Figure 8. **Positional bias in DINOv2 vs. DINOv3.** We visualize the similarity map between a reference keypoint and all target patches using Eq. (16). Darker purple regions indicate low similarity, while brighter yellow regions indicate high similarity. DINOv3 exhibits strong coordinate-aligned artifacts, with bright responses appearing at the same absolute spatial location as the reference keypoint. Our debiasing projection suppresses these spurious activations. We observe that DINOv2 shows much weaker positional bias.

Table 4. **Semantic correspondence on SPair-71k.** PCK@ $T$  (% ,  $\uparrow$ ) for DINOv2 and DINOv3 using original and debiased features. Debiasing produces marginal improvements for DINOv2, but yields substantial gains for DINOv3.

Backbone	Features	PCK@0.05	PCK@0.10	PCK@0.20
<b>DINOv2</b>	original	34.4	50.5	66.8
	debias	<b>34.7</b> (+0.3)	<b>50.8</b> (+0.3)	<b>67.1</b> (+0.3)
<b>DINOv3</b>	original	29.2	45.0	59.8
	debias	<b>32.3</b> (+3.1)	<b>50.0</b> (+5.0)	<b>66.4</b> (+6.6)

aligned artifacts: patches located at the same absolute position as the reference keypoint consistently exhibit strong responses. This phenomenon is more prominent in background regions, where semantic content is scarce or absent, exposing the positional component, which then emerges as spurious activations. After applying the debiasing projection, these position-driven responses are suppressed while the similarity patterns on the object remain stable. This shows that our debiasing suppresses positional bias without degrading the semantic structure encoded in the features. **DINOv2**, in comparison, exhibits weaker positional structure even without any debiasing. The coordinate-aligned patterns characteristic of DINOv3 are mostly absent, and debiasing leads to minor modifications. This contrast suggests that DINOv3 encodes more positional information. We suspect that this could arise as a by-product of its training objective, where the local-consistency constraints and Gram-anchoring may inadvertently amplify absolute spatial correlations in regions with weak semantic cues. The different positional encoding strategy used in DINOv3 compared to DINOv2 may further contribute to this effect.

To quantitatively analyze this behavior, we evaluate semantic correspondence on SPair-71k [42], following the protocol described in Sec. 4.2 of the main paper. This benchmark isolates the *correspondence* component of the representation by measuring cross-image alignment directly on the backbone features, without the overhead of segmentation. As shown in Tab. 4, debiasing yields only small gains for **DINOv2** (all improvements within +0.3 PCK), consistent with its limited positional coupling. In sharp contrast, **DINOv3** benefits substantially, with improvements of +3.1 PCK at  $T = 0.05$ , +5.0 PCK at  $T = 0.10$ , and +6.6 PCK at  $T = 0.20$ . These gains are significant at all thresholds and reflect the removal of positional components that are detrimental for tasks involving feature matching across images.

## A.2. Alternative debiasing strategies

We compare our debiasing scheme against training-free alternatives on COCO-20<sup>i</sup>, reported in Tab. 5. As a baseline, we propose to reduce positional sensitivity by averaging features over multiple augmented views of each image.

Table 5. **Different debiasing strategies.** Comparison of training-free strategies for feature debiasing on COCO-20<sup>i</sup> using mIoU (in % ,  $\uparrow$ ). Augmentations are a viable alternative but require *multiple forward passes*. In contrast our method adds no overhead, except for a single matrix multiplication, since the debiasing projection is pre-computed offline and stored.

Method	mIoU
No debiasing	54.5
Augmentations, 4 views	55.7
Augmentations, 12 views	56.5
<b>Ours</b> (SVD from 1 noise image)	57.6
SVD from 5 noise images	57.7
SVD from 10 noise images	57.7

Concretely, for each image, we sample  $n \in \{4, 12\}$  views using random horizontal and vertical flips as well as homographies. We feed each view independently to DINOv3 and average the corresponding patch features before performing matching and segmentation. This simple strategy already improves over the non-debiased baseline (from 54.5% to 55.7% and 56.5% mIoU for  $n = 4$  and  $n = 12$ , respectively), but *requires  $n$  forward passes per each image* at inference time. In contrast, our projection-based debiasing (SVD from a single noise image) achieves a larger gain (57.6% mIoU) while adding virtually no overhead beyond a single matrix multiplication at inference time. Importantly, our debiasing projection is computed once and stored offline. To test the stability of the estimated positional subspace, we alternatively perform SVD on the features from a small pool of images with *low semantic content*: black, white, horizontal gradient, vertical gradient, and Gaussian noise patterns. Using 5 or 10 such images yields virtually identical results (57.7% mIoU), confirming that the positional subspace is stable and can be captured reliably with a single noise realization.

## A.3. Semantics in debiased feature space

To further examine whether our debiasing projection removes primarily positional variance while preserving the semantic information of the representation, we analyze how semantic information is distributed across principal components in the original and debiased feature spaces. The key idea is simple: in the original DINOv3 representation, positional components account for a substantial amount of variance, causing PCA to allocate some of the leading directions to positional rather than semantic structure. After applying the projection (*cf.* Eq. (4) of the main paper), this positional subspace is removed, reducing the effective rank of the feature representation: although the channel dimensionality remains unchanged, the directions associated with positional variation are collapsed. Therefore, if debiasing removes positional directions, the remaining variance no

longer reflects positional structure, and the resulting principal components predominantly encode semantic variability.

We test this hypothesis by measuring cross-image semantic correspondence accuracy as a function of the retained dimensionality  $d$ . The PCA of original features should degrade earlier when reducing  $d$ , since its components contain a mixture of semantic and positional signals. This experiment complements the analysis in Fig. 7 of the main paper, which focuses on in-context segmentation, by directly probing the effect of debiasing on cross-image feature matching.

The experimental protocol is as follows. For both the *original* and the *debaised* feature spaces, we compute PCA using a separate set of training images, obtaining two orthonormal bases  $\mathbf{U}_{\text{orig}}$  and  $\mathbf{U}_{\text{debias}}$ . This allows us to study how semantic information is distributed when the feature representation is constrained to  $d$  dimensions. For each  $d$  we evaluate:

- **PCA-original.** We compute the PCA basis  $\mathbf{U}_{\text{orig}}$  on original DINOv3 features extracted from COCO-20<sup>i</sup> training images. At test time, target features  $\mathbf{F}$  are projected onto the top- $d$  components:

$$\mathbf{F}_{\text{orig}}^{(d)} = \mathbf{F} \mathbf{U}_{\text{orig}}[:, 1:d]. \quad (17)$$

- **Debias+PCA.** We first apply our positional debiasing projection to the same COCO-20<sup>i</sup> training features, then compute a PCA basis  $\mathbf{U}_{\text{debias}}$  in this debaised space. At test time, features are first debaised, then projected onto the top- $d$  PCA components:

$$\tilde{\mathbf{F}}_{\text{PCA}}^{(d)} = \tilde{\mathbf{F}} \mathbf{U}_{\text{debias}}[:, 1:d]. \quad (18)$$

Semantic correspondence is evaluated on SPair-71k, isolating cross-image alignment from segmentation, by using these two  $d$ -dimensional representations. Results are plotted in Fig. 9. Across all dimensionalities, the PCA-debaised curve remains consistently above the PCA-original. This shows that the variance removed by our projection does not encode meaningful semantic information. Once positional variance is eliminated, the remaining dimensions form a cleaner and more stable semantic subspace. In contrast, the leading components of the *original* features also capture structured positional signals, resulting in consistently lower correspondence accuracy. In particular, at  $d = 32$ , the plot shows a gap of +7.8 PCK@0.10. As  $d$  increases, both representations approach their full-dimensional capacity, and the gap converges to +2.8 PCK@0.10. While this experiment does not establish that *all* positional biases are removed, it provides clear evidence that the directions suppressed by our debiasing are not useful for identifying semantic correspondences, and that the resulting representation supports more reliable matching across a wide range of dimensionalities.

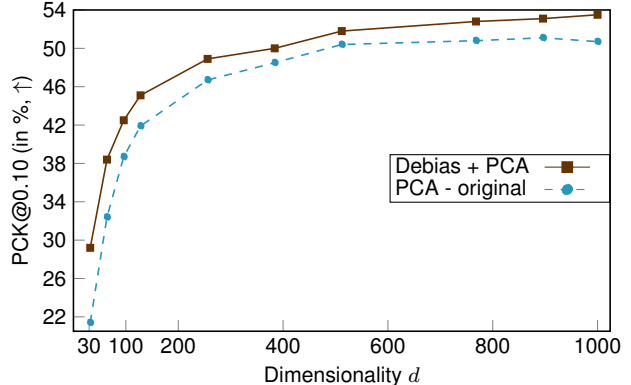


Figure 9. **Debaised features preserve semantic structure.** We compute PCA bases on COCO training images for (i) the original DINOv3 features and (ii) our debaised features. We then project both representations to  $d$  principal components and evaluate semantic correspondence (PCK@0.10) on SPair-71k. Across all  $d$ , Debias + PCA consistently outperforms PCA-original, indicating that the removed directions primarily encode positional bias. After debiasing, the remaining variance concentrates around semantic structure, yielding better results when compressed via PCA.

Table 6. **Hyperparameter overview.** INSID3 uses only three hyperparameters, all fixed across datasets, for both semantic, part, and personalized segmentation.

Hyperparameter	Value
$\tau$ (clustering sensitivity)	0.6
$\alpha$ (aggregation threshold)	0.2
$s$ (debias rank)	500

#### A.4. Discussion

We proposed a simple approach for removing positional biases from dense features of DINOv3. We demonstrate that debaised features aid accuracy for cross-image matching. Still, positional information remains a trade-off. While positional information can support approaching certain tasks, strong absolute positional biases can hamper cross-image correspondence. For example, in semantic segmentation, predicting sky can benefit from absolute positional information, whereas correspondence tasks require features that generalize across spatial positioning. Existing work in different domains also removed absolute positional information explicitly or implicitly from dense features by exploiting equivariance across augmented views [76, 79, 81] or multi-view consistency [32, 80, 82]. Different from these approaches, our approach does not require any training and provides a flexible, efficient, and simple decomposition between semantic features and absolute positional encoding.

Table 7. **Comparison of INSID3 (mIoU in %,  $\uparrow$ ) on 5-shot semantic and part segmentation.** Models are provided with 5 contextual examples and tasked with segmenting the annotated concept in the target image. INSID3 scales effectively to multiple references, achieving robust performance across domains. All hyperparameters are reused from the 1-shot setting without any tuning, highlighting the versatility of our approach. Gray indicates the model was trained on the corresponding train split of the dataset; best results **bold**, 2<sup>nd</sup> best underlined.  $\dagger$  denotes a GF-SAM variant using DINOv3 features.

Method	Encoder	#Param	Semantic						Part		
			LVIS-92 <sup>i</sup>	COCO-20 <sup>i</sup>	ISIC	SUIM	iSAID	X-Ray	PASCAL	PACO	Avg
<b>Task-specific fine-tuning: <i>Semantic + mask supervision</i></b>											
SegGPT [64]	ViT	354 M	25.4	67.9	45.2	33.7	35.9	<b>89.1</b>	42.8	14.1	44.3
SINE [38]	DINOv2	373 M	35.5	66.1	28.6	54.8	40.5	40.6	36.4	25.4	41.0
DiffuS [74]	Stable Diffusion	890 M	35.4	72.2	32.7	49.8	48.0	45.1	39.7	26.1	43.6
<b>Training free: <i>Mask-supervised pre-training</i></b>											
Matcher [39]	DINOv2 + SAM	945 M	40.0	60.7	35.0	50.6	34.3	71.2	45.8	33.6	46.4
GF-SAM [69]	DINOv2 + SAM	945 M	<u>44.2</u>	<b>66.8</b>	55.2	58.1	52.4	52.9	51.2	<u>41.9</u>	52.8
GF-SAM <sup>†</sup> [69]	DINOv3 + SAM	945 M	42.8	64.4	56.7	58.6	53.2	54.7	50.3	39.3	52.5
$\hookrightarrow$ + <i>our debias</i>	DINOv3 + SAM	945 M	43.6	64.6	<u>58.2</u>	<u>59.2</u>	<u>54.1</u>	59.1	<u>51.4</u>	40.2	<u>53.8</u>
<b>Training free: <i>Unsupervised pre-training</i></b>											
INSID3 ( <i>ours</i> )	DINOv3	<b>304 M</b>	<b>47.2</b>	<u>65.1</u>	<b>63.9</b>	<b>61.7</b>	<b>56.9</b>	<u>80.1</u>	<b>57.1</b>	<b>46.8</b>	<b>59.9</b>

## B. Implementation details

INSID3 relies on only three scalar hyperparameters, summarized in Tab. 6. All hyperparameters are selected once on the COCO-20<sup>i</sup> training split using a  $k$ -fold cross-validation procedure (with  $k = 3$ ), and are kept *fixed across all datasets, domains, and tasks* (semantic, part, and personalized segmentation). No dataset-specific or task-specific tuning is performed. The clustering sensitivity  $\tau$  controls the granularity of the agglomerative clustering step. We choose a value ( $\tau = 0.6$ ) that provides fine-grained clusters at part level, and rely on aggregation based on similarity with the in-context example to merge clusters to the desired granularity. The aggregation threshold  $\alpha$  determines how strictly clusters must agree semantically and structurally with the seed region; the debiasing rank  $s$  specifies the number of positional directions removed by our projection. Despite their simplicity, these three values generalize well across all experiments, highlighting the stability of the method.

## C. Additional Experiments

Here, we provide additional experimental results, complementing Sec. 4 of the main paper.

### C.1. $k$ -shot segmentation

Although our main experiments evaluate INSID3 under the 1-shot segmentation setting, our approach naturally extends to multiple reference examples. Let  $\{(\mathbf{I}^{r_m}, \mathbf{M}^{r_m})\}_{m=1}^k$  denote the  $k$  reference images and masks of the  $k$ -shot setting. The clustering of the target image (Sec. 3.2) and the aggregation procedure (Sec. 3.4) remain unchanged. Only the correspondence stage (Sec. 3.3) requires adaptation.

For each target patch  $i$ , we compute its nearest neighbor

in every reference image using the debiased features:

$$\text{NN}_m(i) = \arg \max_{j \in \Omega} (\tilde{\mathbf{F}}_i^t, \tilde{\mathbf{F}}_j^{r_m}). \quad (15)$$

A patch is retained as a valid candidate if its nearest neighbor in the reference lies within the mask for a majority of the reference images, *i.e.*,

$$\left| \{m \mid \mathbf{M}_{\text{NN}_m(i)}^{r_m} = 1\} \right| \geq \left\lceil \frac{k}{2} \right\rceil. \quad (19)$$

This majority-vote filtering keeps only correspondences consistently supported across references. For prototype construction, we compute one debiased prototype per reference, and then average them:

$$\tilde{\mathbf{p}}^r = \frac{1}{k} \sum_{m=1}^k \tilde{\mathbf{p}}^{r_m}. \quad (20)$$

The aggregated prototype is plugged into Eq. (10) to compute cross-image similarity for each target cluster, which drives seed selection and subsequent aggregation. We follow standard few-shot segmentation protocols and evaluate the case  $k = 5$  in Tab. 7.

**Discussion.** We observe that INSID3 benefits consistently from additional reference examples. Moving from the 1-shot to the 5-shot setting, our method yields substantial gains across all benchmarks (*cf.* Tabs. 1 & 7), with improvements in the range of +1.3–9.5 % pts. mIoU. Overall, INSID3 achieves the best average score with a gain over the best competitor of +6.1 % points. In particular, INSID3 outperforms GF-SAM by +3.0 % pts. mIoU on the challenging LVIS-92<sup>i</sup>, and by 5.4 % pts. on average on Part segmentation. On challenging datasets from the medical domain, the

Table 8. **Backbone analysis for INSID3.** We report mIoU (in %,  $\uparrow$ ) on COCO-20<sup>i</sup> of INSID3 with different backbone features. DINOv3 features lead to the best segmentation accuracy.

DINOv3	DINOv2	Franca	Perception Enc.	Stable Diff.
<b>57.6</b>	45.1	39.2	48.4	33.2

gain is +8.7 % and +27.2 % pts. on ISIC and X-Ray, respectively. On SUIM the performance boost is +3.6 % pts., and +4.5 % pts. mIoU on the remote-sensing domain of iSAID. Only on COCO, INSID3 incurs in a small gap of  $-1.7$  % pts. Notably, our proposed debiasing strategy also improves the baseline of GF-SAM where DINOv3 is used as encoder, providing an improvement of +1.0 % pts. over the original method with DINOv2. Overall, the table reveals a trend consistent with the 1-shot setting: fine-tuned methods struggle to generalize when the test distribution deviates from the training distribution. Even when excluding the challenging medical and remote-sensing datasets, models fine-tuned on COCO exhibit a substantial accuracy drop on LVIS, whose long-tailed taxonomy differs from that of COCO. In contrast, training-free approaches avoid these pitfalls, offering stronger generalization across tasks and datasets without requiring domain-specific adaptation. Among them, our method stands out by leveraging only self-supervised DINOv3 features, yet achieving results that are competitive with or superior to methods relying on explicit mask-level supervision. Importantly, these 5-shot results are obtained *without* introducing any new components or tuning additional hyperparameters: we reuse exactly the same encoder, clustering configuration, and aggregation thresholds as in the 1-shot experiments, and only replace the correspondence stage with the simple majority-vote and prototype averaging scheme in Sec. C.1. This shows that INSID3 scales to multiple references in a strictly plug-and-play manner, and that its training-free design can effectively integrate complementary in-context signals without dataset- or shot-specific adaptation.

## C.2. Dense representations matter

A central motivation of our work is that earlier ICS methods had to *compensate* for the limited spatial structure of existing VFM features, either by training segmentation decoders [41], fine-tuning diffusion models [74], or coupling DINOv2 with SAM for mask generation [39, 69]. These components were introduced because prior VFMs did not simultaneously provide (i) reliable semantic correspondence across images and (ii) sufficiently dense, part-aware structure within a single image. We validate this argument directly by replacing DINOv3 with other VFMs. In particular, we use features from DINOv2 [47], Franca [78], Perception Encoder [2], and Stable Diffusion 2.1 [52]. We apply INSID3 without any algorithmic changes, and tune hyperpa-

Table 9. **Comparison with SAM3.** We compare INSID3 to Segment Anything 3 (SAM 3) on COCO-20<sup>i</sup> using mIoU (in %,  $\uparrow$ ). We evaluate two adaptations of SAM 3: (i) a *video-style* formulation, where reference and target are treated as consecutive frames and the mask is propagated, and (ii) an *image concatenation* strategy, where images are combined horizontally and prompted.

Method	mIoU
<b>Training free: Mask-supervised pre-training</b>	
Segment Anything 3 (video-style propagation)	26.7
Segment Anything 3 (image concatenation)	52.9
<b>Training free: Unsupervised pre-training</b>	
<b>INSID3 (ours)</b>	<b>57.6</b>

rameters for each backbone (*cf.* Tab. 8). Segmentation accuracy of all other VFMs drops significantly on COCO-20<sup>i</sup> over DINOv3. These results support a key observation: DINOv3 self-supervised representations jointly exhibit strong semantic structure and spatially localized, dense features, which together are sufficient for ICS to arise from a single frozen backbone without decoders, fine-tuning, or external models.

## C.3. Comparison with SAM 3

We further compare INSID3 with the recent Segment Anything 3 (SAM 3) model [75], a foundation model for promptable segmentation that supports multiple input modalities, including points, masks, and text prompts. Among its capabilities, SAM 3 enables *visual prompting*, where a mask provided on an object can be used to segment other instances of the same concept *within the same image*. In this experiment, we investigate whether such visual prompting can generalize across *different* images, *i.e.* from a reference to a target, to solve in-context segmentation. Since SAM 3 is not natively designed for this setting, we consider two adaptations. First, following prior work [12], we adopt a *video-style* formulation, where the reference and target images are treated as consecutive frames and the mask is propagated from the reference (first frame) to the target. Second, we propose an *image concatenation* strategy, where the reference and target are stacked horizontally into a single image and the mask is provided on the reference region. Results on COCO-20<sup>i</sup> are reported in Tab. 9. We observe that the image concatenation strategy significantly outperforms the video-style propagation, achieving 52.9 % mIoU compared to a lower accuracy of 26.7 %, respectively. Notably, INSID3 attains 57.6 % mIoU, outperforming SAM3 by 4.7 percentage points despite not relying on any segmentation supervision.

## C.4. Corner case: Empty mask

The standard in-context segmentation formulation assumes that the reference concept is present in the target image.

Table 10. **Absence of the reference concept.** Percentage of correct empty-mask predictions ( $\%$ ,  $\uparrow$ ) when the target image does not contain the prompted object (COCO, 4 000 pairs). *n.a.*: methods that always return a non-empty mask (*i.e.*, 0 % in practice).

Method	Correct empty predictions (in %) $\uparrow$
<b>Task-specific fine-tuning: <i>Semantic + mask supervision</i></b>	
SegGPT [64]	79
SegIC [41]	36
<b>Training free: <i>Mask-supervised pre-training</i></b>	
PerSAM [72]	<i>n.a.</i>
Matcher [39]	<i>n.a.</i>
GF-SAM [69]	<i>n.a.</i>
<b>Training free: <i>Unsupervised pre-training</i></b>	
<b>INSID3 (ours)</b>	<b>85</b>

Table 11. **Computational analysis** of INSID3 vs. previous methods in milliseconds (ms,  $\downarrow$ ). Inference time is measured for a single in-context example (*i.e.*, example and target image). Runtime is measured on a single RTX 4090.

Method	Backbone	Resolution	Runtime $\downarrow$
<b>Task-specific fine-tuning: <i>Semantic + mask supervision</i></b>			
SegGPT [64]	ViT	640 <sup>2</sup>	110 ms
SegIC [41]	DINOv2	896 <sup>2</sup>	301 ms
<b>Training free: <i>Mask-supervised pre-training</i></b>			
PerSAM [72]	SAM	1024 <sup>2</sup>	504 ms
Matcher [39]	DINOv2 + SAM	1024 <sup>2</sup>	9 000 ms
GF-SAM [69]	DINOv2 + SAM	1024 <sup>2</sup>	1 030 ms
<b>Training free: <i>Unsupervised pre-training</i></b>			
<b>INSID3 (ours)</b>	DINOv3	1024 <sup>2</sup>	<b>302 ms</b>

However, a practical use case arises when the target image does not contain the object specified by the reference prompt, in which case the desired output is an empty mask. INSID3 can naturally accommodate this case by also subjecting the seed cluster to the aggregation criterion (*cf.* Eq. 12). When the concept is absent, cross-image similarity scores remain uniformly low, and no cluster satisfies the selection criterion, resulting in an empty prediction.

To evaluate this setting, we construct 4 000 reference-target pairs from COCO (80 classes), where the target image does not contain the reference concept. Table 10 reports the percentage of correct empty predictions. INSID3 correctly predicts empty masks in 85% of cases. Methods based on SAM [39, 69, 72] cannot produce empty outputs by design and therefore always return a non-empty mask. Compared to supervised approaches, INSID3 outperforms SegIC [41] and SegGPT [64] despite requiring no task-specific training.

Table 12. **Detailed computational analysis of INSID3.** We report inference time of each component in milliseconds (ms,  $\downarrow$ ). Inference time is measured for a single in-context example. Runtime measured on a single RTX 4090.

Component	Runtime $\downarrow$
Encoder forward + debiasing	78 ms
Compute similarity + cluster scoring	3 ms
Clustering	166 ms
CRF refinement	55 ms
<b>Total inference time</b>	<b>302 ms</b>

Table 13. **Computational analysis for different resolutions.** We report inference time of INSID3 for different resolution in milliseconds (ms,  $\downarrow$ ). Inference time is measured for a single in-context example. Runtime measured on a single RTX 3090.

<i>Low resolution</i> $\leftarrow$ <b>Runtime of INSID3</b> $\rightarrow$ <i>High resolution</i>						
512 px	720 px	896 px	1 024 px	1 440 px	1 600 px	1 760 px
93 ms	180 ms	230 ms	302 ms	689 ms	930 ms	1 102 ms

## D. Computational Cost of INSID3

Table 11 reports the inference speed of INSID3 compared to training-free and fined-tuned baselines. INSID3 provides a significantly faster inference runtime than existing training-free approaches. This efficiency follows directly from our *single-backbone design*. In contrast, SAM-based pipelines separate the problem into two stages: DINOv2 is used to compute semantic correspondences, and SAM is prompted to produce masks. Because these two models operate in different feature spaces, semantic matching and mask generation are decoupled and must be coordinated through additional steps (*e.g.*, point selection, prompt engineering, mask filtering, and scoring). This multi-stage interaction results in significant inference overhead.

In contrast, INSID3 performs both semantic alignment and mask generation directly in the DINOv3 feature space. On a single RTX 4090, INSID3 runs at 302 ms, compared to 1 030 ms for GF-SAM, the most competitive baseline w.r.t. downstream accuracy. The detailed runtime breakdown (*cf.* Tab. 12) shows that the dominant cost of INSID3 is agglomerative clustering (166 ms), with the DINOv3 forward pass and debiasing accounting for 78 ms. Similarity computation and cluster scoring are negligible (3 ms). We use a GPU-accelerated dense CRF [77] for refinement (55 ms). Although agglomerative clustering has quadratic complexity in the number of tokens, INSID3 nevertheless scales well in practice to higher image resolutions (*cf.* Table 13). Notably, INSID3 at 1 760  $\times$  1 760 remains comparable in runtime to GF-SAM at 1 024  $\times$  1 024. Overall, INSID3 remains computationally efficient by operating entirely within a single feature space, without relying on auxiliary segmenta-



tation, one could instead provide an example object in the reference image and ask the model to segment the corresponding instances in the target image separately, rather than merging them into a single semantic mask. In our observations, clusters belonging to the same instance often exhibit stronger mutual similarity than clusters from different instances. Exploiting these affinities to iteratively recover multiple instances, for example by expanding a seed with its most similar clusters and then re-seeding on the remaining regions, is an interesting direction for future work. Finally, INSID3 relies on the semantic structure encoded in frozen self-supervised features of DINOv3. Although our debiasing improves cross-image matching, the quality of the final segmentation still depends on the representational properties of the underlying backbone, suggesting that future advances in self-supervised representations could further strengthen this paradigm.

## References

- [75] Nicolas Carion, Laura Gustafson, Yuan-Ting Hu, Shoubhik Debnath et al. SAM 3: Segment anything with concepts. *arXiv:2511.16719 [cs.CV]*, 2025. [v](#)
- [76] Stephanie Fu, Mark Hamilton, Laura E. Brandt, Axel Feldmann, Zhoutong Zhang, and William T. Freeman. FeatUp: A model-agnostic framework for features at any resolution. In *ICLR*, 2024. [iii](#)
- [77] Đ.Khuê Lê-Huu and Karteek Alahari. Regularized Frank-Wolfe for dense CRFs: Generalizing mean field and beyond. In *NeurIPS*, pages 1453–1467, 2021. [vi](#)
- [78] Shashanka Venkataramanan, Valentin Pariza, Mohammadreza Salehi, Lukas Knobel, Spyros Gidaris, Elias Ramzi, Andrei Bursuc, and Yuki M. Asano. Franca: Nested Matrioshka clustering for scalable visual representation learning. *arXiv:2507.14137 [cs.CV]*, 2025. [v](#)
- [79] Thomas Wimmer, Prune Truong, Marie-Julie Rakotosaona, Michael Oechsle, Federico Tombari, Bernt Schiele, and Jan Eric Lenssen. AnyUp: Universal feature upsampling. In *ICLR*, 2026. [iii](#)
- [80] Jiawei Yang, Boris Ivanovic, Or Litany, Xinshuo Weng, Seung Wook Kim, Boyi Li, Tong Che, Danfei Xu, Sanja Fidler, Marco Pavone, and Yue Wang. EmerNeRF: Emergent spatial-temporal scene decomposition via self-supervision. In *ICLR*, 2024. [iii](#)
- [81] Jiawei Yang, Katie Z. Luo, Jiefeng Li, Congyue Deng, Leonidas Guibas, Dilip Krishnan, Kilian Q. Weinberger, Yonglong Tian, and Yue Wang. Denoising vision transformers. In *ECCV*, volume 85, pages 453–469, 2024. [iii](#)
- [82] Yuanwen Yue, Anurag Das, Francis Engelmann, Siyu Tang, and Jan Eric Lenssen. Improving 2D feature representations by 3D-aware fine-tuning. In *ECCV*, volume 2, pages 57–74, 2024. [iii](#)